Acoustically powered surface-slipping mobile microrobots

Amirreza Aghakhani[a,1], Oncay Yasa[a,1], Paul Wrede[a], and Metin Sitti[a,b,c,2]

[a]Physical Intelligence Department, Max Planck Institute for Intelligent Systems, 70569 Stuttgart, Germany; [b]School of Medicine, Koç University, 34450 Istanbul, Turkey; and [c]School of Engineering, Koç University, 34450 Istanbul, Turkey

Edited by John A. Rogers, Northwestern University, Evanston, IL, and approved December 30, 2019 (received for review November 14, 2019)

Untethered synthetic microrobots have significant potential to revolutionize minimally invasive medical interventions in the future. However, their relatively slow speed and low controllability near surfaces typically are some of the barriers standing in the way of their medical applications. Here, we introduce acoustically powered microrobots with a fast, unidirectional surface-slipping locomotion on both flat and curved surfaces. The proposed three-dimensionally printed, bullet-shaped microrobot contains a spherical air bubble trapped inside its internal body cavity, where the bubble is resonated using acoustic waves. The net fluidic flow due to the bubble oscillation orients the microrobot's axisymmetric axis perpendicular to the wall and then propels it laterally at very high speeds (up to 90 body lengths per second with a body length of 25 μm) while inducing an attractive force toward the wall. To achieve unidirectional locomotion, a small fin is added to the microrobot's cylindrical body surface, which biases the propulsion direction. For motion direction control, the microrobots are coated anisotropically with a soft magnetic nanofilm layer, allowing steering under a uniform magnetic field. Finally, surface locomotion capability of the microrobots is demonstrated inside a three-dimensional circular cross-sectional microchannel under acoustic actuation. Overall, the combination of acoustic powering and magnetic steering can be effectively utilized to actuate and navigate these microrobots in confined and hard-to-reach body location areas in a minimally invasive fashion.

microrobots | acoustic actuation | magnetic control | microswimmers | bubble oscillation

Untethered synthetic microrobots have been recently investigated for their potential applications in targeted drug delivery, detoxification, and noninvasive surgeries (1–4). The existing microswimmers are powered by different external energy sources, such as light (5–7), electrical (8, 9), magnetic (10, 11), and acoustic (12, 13) fields, or fueled by chemicals in the environment (14, 15). Among these actuation schemes, magnetic and acoustic field-based powering methods are the most prevalent in the biomedical context thanks to their deep-tissue penetration and high-energy-density capabilities. While the acoustic waves can deliver strong propulsion forces (16), the magnetic field can provide controlled steering of the microswimmers (17, 18). For example, acoustically excited bubbles can generate high streaming forces (16, 19), and when employed in the robot's body they can act as an engine for the propulsion (12, 20).

Up to now, a few studies have used two-dimensional (2D) microfabrication (20, 21) and ultraviolet light-based polymerization techniques (12, 22) to fabricate around 100- to 300-μm microrobots with cylindrical or conical cavities for bubble entrapment. As the bubble diameter scales down to the 10- to 30-μm range, the cylindrical cavity geometry would require advanced hydrophobic treatment to hold a microbubble stable due to the increased surface tension forces (19). Therefore, advanced three-dimensional (3D) microfabrication techniques could be used to create spherical voids inside the swimmer's body to increase the stability of a trapped air bubble (23). Previously, Louf et al. (13) demonstrated a hovering microswimmer by trapping a microbubble underneath its body, facing toward the substrate. The swimming motion was achieved by the acoustic radiation force of two ultrasound transducers, while the acoustic streaming of the microbubble was utilized for reducing the adhesion. However, the locomotion was limited to flat substrates and the directionality of motion was not clear since the microswimmer was not exactly pushed away from the transducers. Most recently, Ren et al. (24) demonstrated bubble-based acoustic microswimmers for particle and cell manipulation. Their microswimmer design allowed self-alignment at the boundaries, swimming and climbing on solid boundaries. However, the propulsion method in that study required simultaneous application of acoustic and magnetic fields. Moreover, their cylindrical cavity design required hydrophobic surface modification to stabilize the bubble during acoustic actuation. In general, the locomotion behavior of bubble-based microrobots in a low-Reynolds flow regime is complex, especially when the microbubble is below the 30-μm range and oscillates near solid walls, due to the nonlinear acoustic forces (23). The interaction of such acoustically powered microrobots near walls has not been fully investigated yet and therefore their directionality control remains a challenge.

Here, we propose a type of microbubble-based acoustic microrobot based on a surface-slipping mechanism. Under the acoustically induced bubble oscillation, the microrobot flips automatically toward the substrate, and the steady streaming flows around the body create a net flux, which results in the slipping motion. To enable a unidirectional motion, we introduced a structural anisotropy

Significance

Untethered microrobots have significant applications in medical interventions such as targeted drug delivery. Here, we present an acoustically propelled microrobot that uses a fast and unidirectional surface-slipping locomotion strategy to navigate on both flat and curved surfaces. The three-dimensionally microprinted microrobot contains a trapped spherical air bubble to harness acoustic waves for propulsion at incredibly high speeds, up to 90 body lengths per second with body length of about 25 μm, and it can be steered by external magnetic fields. The proposed microrobot has a thrust force of about two to three orders of magnitude higher than that of microorganisms, such as algae and bacteria, which is sufficient for navigation inside vascular capillaries with blood flow.

Author contributions: A.A. and M.S. designed research; A.A., O.Y., and P.W. performed research; A.A. and O.Y. analyzed data; A.A., O.Y., P.W., and M.S. wrote the paper; A.A. conducted simulations; and M.S. supervised the research.

The authors declare no competing interest.

This article is a PNAS Direct Submission.

[1]A.A. and O.Y. contributed equally to this work.

[2]To whom correspondence may be addressed. Email: sitti@is.mpg.de.

This article contains supporting information online at https://www.pnas.org/lookup/suppl/doi:10.1073/pnas.1920099117/-/DCSupplemental.

First published February 3, 2020.

"fin" on the microrobot's cylindrical body, which passively biases the bubble-induced streaming pattern and hence the locomotion direction. Further, to enable steering control, we coated the microrobot anisotropically with a nickel nanofilm and applied a uniform magnetic field to change the propulsion direction. We also demonstrated the cargo-trapping, transport, and release functionalities of the microswimmer by tuning the amplitude of the acoustic waves. Finally, we showed the locomotion capability of the microrobot in 3D circular microchannels against gravity.

Results

Microrobot Design and Fabrication. We fabricated the microrobots using the two-photon polymerization technique, that is, 3D microprinting, as shown in Fig. 1*A*. The geometry of the microrobot is in the form of a cylinder with a hemispherical dome 24 μm in diameter. The acoustic microrobot comprises a spherical void at the center of its polymeric body with an orifice facing the cylinder base. When immersed in a fluid medium, an air bubble forms and stays intact inside the cavity due to the surface tension without any necessity of hydrophobic treatment (Fig. 1 *A*, *Inset*). Fig. 1*B* depicts the surface-slipping locomotion mechanism of the proposed microrobot with a "fin" in our design, which adds an anisotropy in the symmetrical body shape. Under ultrasound actuation, the microrobot flips toward the substrate and starts slipping to the desired distance. We tested two designs, a fully symmetric microrobot (Fig. 1*C*) as a control and a microrobot with a fin (Fig. 1*D*). To test the quality of the 3D-printed microrobots, we performed scanning electron microscopy characterizations as shown in Fig. 1 *C* and *D*. Under ultrasound actuation, the symmetrical and anisotropic microrobots swim differently. Fig. 1*E* shows the random trochoidal swimming path of the fully symmetric design, due to both translation and rotation of the microrobot. However, by adding a fin, the microrobot can swim in a forward direction, as shown in Fig. 1*F* and Movie S1. Hereafter, we focus on the microrobot with the fin and characterize the resonance frequency and swimming behavior.

Characterization of the Microbubble Resonance Frequency and Stability. The acoustic microrobot is composed of a spherical cavity reinforced with a polymeric shell with an opening nozzle. When the microrobot is immersed in the liquid-filled chamber, an air bubble immediately becomes trapped inside the cavity and stays intact in a spherical form (Fig. 2 *A*, *i*). The excess static pressure of the air bubble, which is balanced by the surface tension force, is known as the Laplace pressure (19). In our microrobot design, however, the only area of the bubble that is exposed to the surface tension force at the liquid–air interface is the orifice part; the rest of the bubble surface is confined by the polymeric shell and hence experiences no normal stress. In order to characterize the resonant frequency of the entrapped microbubble we performed frequency sweep tests using an acoustic apparatus, shown in Fig. 2*A*. The microchannel was made of acoustically transparent polydimethylsiloxane (PDMS) material, which allows traveling wave-based acoustic actuation and avoids the generation of standing waves inside the chamber. We filled the PDMS channel with phosphate-buffered saline (PBS) medium and 2-μm-diameter polystyrene (PS) beads and measured the microstreaming flow speed in front of the microrobot using a custom-made particle tracing velocimetry algorithm.

Two piezoelectric transducers were attached adjacent to the chamber: one for sending the acoustic waves and the other for sensing the vibrational signal. Under acoustic actuation at different frequencies, a vortex flow is generated in front of the microrobot, which is the combination of two phenomena: 1) the Eckart streaming or so-called quartz wind, which is the flow resulting from the dissipation of the acoustic energy into the bulk fluid medium (25), and 2) steady streaming flow near the oscillating boundary layer of the microbubble at the liquid–air interface (26, 27). However, at the length scale of our microrobot (denoted by l) and the excitation frequency range around 300 kHz, the acoustic wavelength ($\lambda \gg l$) and the attenuation length ($\propto \frac{1}{f^2}$) are large enough that the effect of Eckart streaming can be neglected (28, 29). Therefore, by sweeping the sound wave frequencies in our setup (shown in Fig. 2*A*) we found the resonant frequency of the microbubble to be around 327 kHz. Fig. 2*D* presents the average velocity of the microbeads normalized to the sensing voltage as a function of the excitation frequency. Fig. 2*B* shows the microstreaming pattern in front of the microrobot at resonance (Movie S2), generated by overlaying the trajectories of microbeads. The microstreaming patterns at different frequencies are also shown in *SI Appendix*, Fig. S3.

We performed numerical simulations to obtain the acoustic resonant frequency of the spherical air bubble with the supporting polymer shell immersed in a quiescent liquid medium (details are given in *SI Appendix*, section S1). Fig. 2*C* demonstrates the acoustic pressure map of the microbubble at the computed resonant frequency of 305 kHz. We attribute the shift between the experimental and numerical resonant frequency of the microbubble to the surface tension-induced stiffness component, which is missing in the simulation environment (*SI Appendix*, section S2). Unlike other reported bubble-based swimmers in the literature (12, 22, 30) with bubble radius bigger than 30 μm, at scales related to our design the effect of surface tension is significant. Indeed, using a scaling analysis, we found that the ratio of surface tension to volumetric pressure change is around 3 (*SI Appendix*, section S2).

After characterizing the resonant frequency of the microbubbles we performed a set of experiments to investigate the bubble's stability during acoustic actuation. In order to emphasize the importance of the spherical cavity design in stabilizing the entrapped air bubble, we fabricated similar microrobots with a cylindrical cavity structure. Without any hydrophobic surface treatment on the structures, we could observe that each microbubble inside the microrobots with a spherical cavity was stable under continuous acoustic exposure for at least 5 h. However, all of the microbubbles inside the microrobots with cylindrical cavity structures dissolved in the fluidic medium shortly after 8 min. The time lapse of the bubble stability tests is presented in *SI Appendix*, Fig. S5 and Movie S3.

Mechanism of Propulsion and Surface Slipping. After releasing the acoustic microrobots inside the PDMS chamber, the traveling acoustic waves at their resonant frequency causes the bubble to oscillate with a small amplitude of ϵ. Under acoustic actuation, the freed microrobot propels due to combined effects of the acoustic radiation force (31) resulting from the scattering of the acoustic waves on the polymeric shell and the steady streaming of the bubble at the unconfined surface. However, the propulsion force from bubble streaming is much higher than that resulting from the acoustic radiation force (*SI Appendix*, section S4). In addition, since the bubbles oscillate at a much longer wavelength than their radii, the microrobots experience the same ultrasound pressure within the acoustic beam width of about the wavelength. For instance, for the bubble radius of 9 μm in this work oscillating at 330 kHz, the acoustic wavelength is about 4.5 mm in a water medium. On the other hand, the penetration depth of the acoustic beam depends on the transducer radius (a) and the wavelength (λ) by $L \sim a^2/\lambda$, where L is the near-field focal length (32). For example, for the transducer radius ranging from 1 to 3 cm, the penetration depth is between 2 and 20 cm. This range could be sufficient for most of the potential medical applications of the microrobots.

Notably, under the periodic oscillation of the microbubble the microstreaming flow is highly dependent on its distance from the solid substrate. In fact, Doinikov and Bouakaz (33) theoretically predicted that the streaming motion is enhanced by the presence of a rigid wall. More recently, Bertin et al. (23)

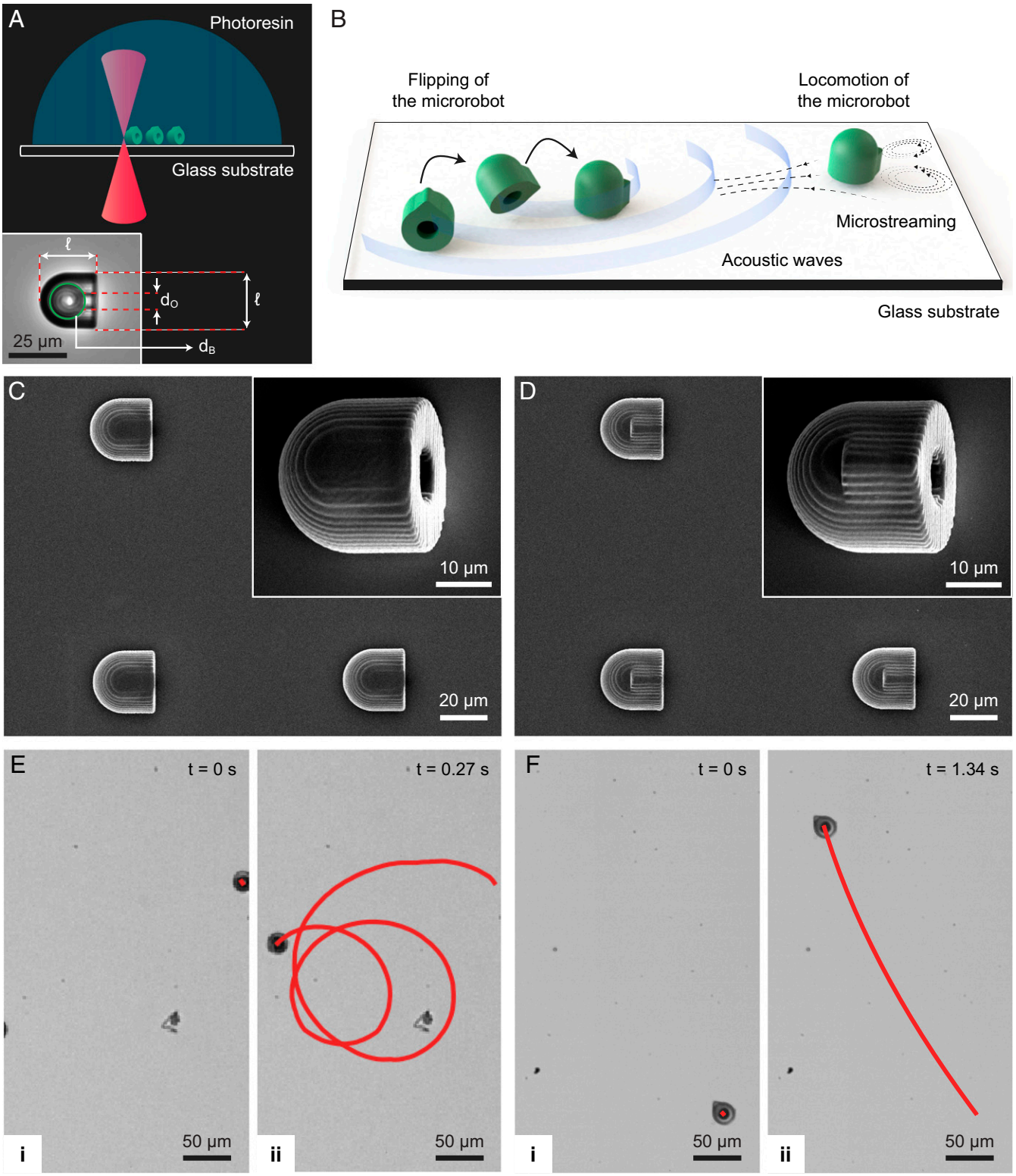

Fig. 1. Fabrication and propulsion behavior of the proposed acoustic microrobots. (*A*) Three-dimensional nanoprinting of the microrobot on a glass slide using the two-photon lithography technique. (*Inset*) The fabricated microrobot immersed in water, where d_B and d_O are the diameters of the air bubble and orifice, respectively, and *l* is the length. (*B*) Schematics of the robot propulsion, where under the acoustic waves the robot flips toward the substrate and slips forward due to the asymmetric microstreaming pattern generated by the pulsating microbubble and the designed "fin" structure. (*C* and *D*) Scanning electron microscopy images of the fully symmetric and anisotropic microrobot designs. (*E*) The trochoidal random propulsion path example of the symmetric microrobot under ultrasound actuation from (*i*) t = 0 s to (*ii*) t = 0.27 s, which results from the combined translation and rotation of the body. (*F*) The directional forward motion example of the microrobot with a fin structure from (*i*) t = 0 s to (*ii*) t = 1.34 s, under ultrasound actuation. The introduction of the fin is crucial for creating the flow asymmetry, which allows the unidirectional motion (Movie S1).

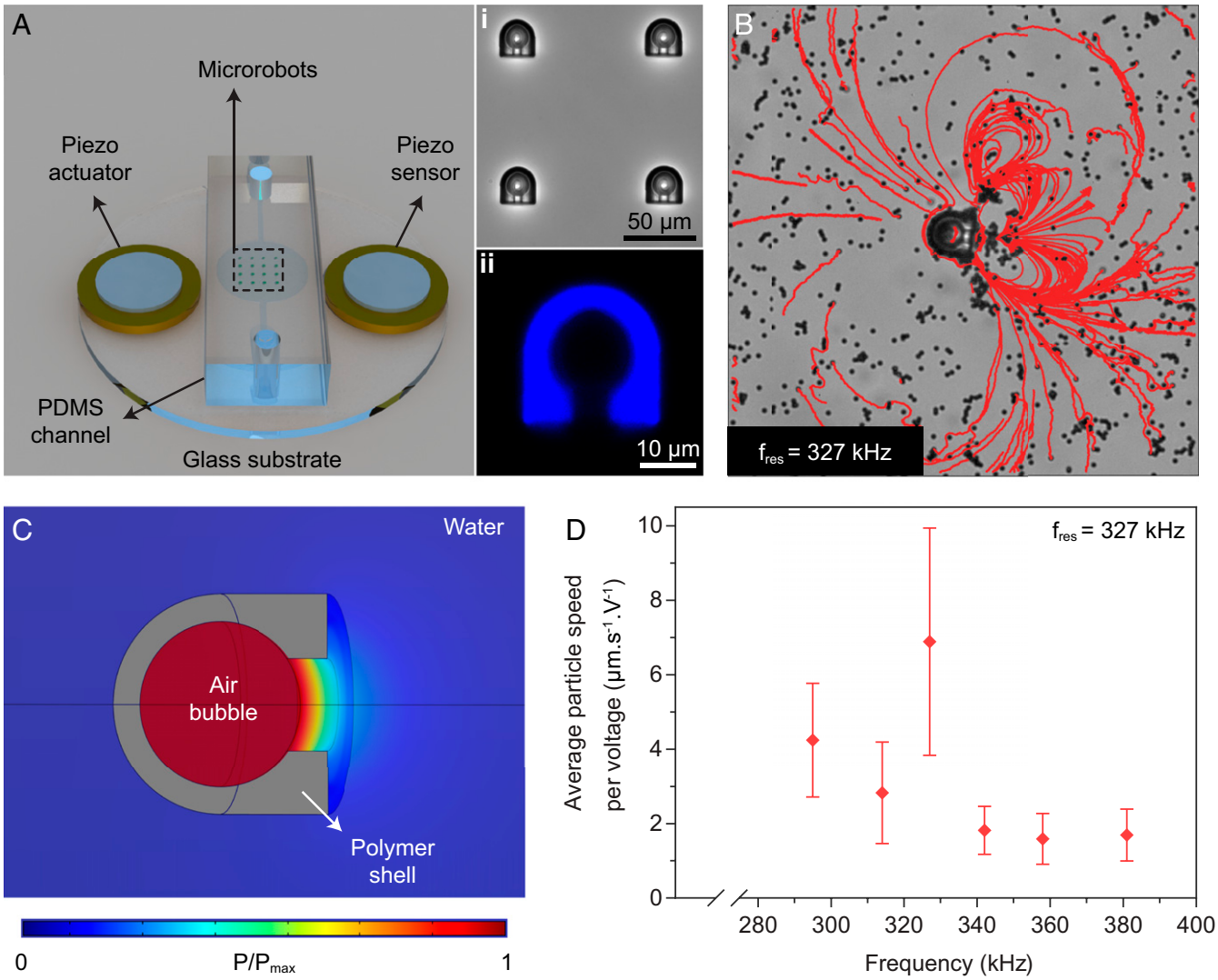

Fig. 2. Characterization of the resonance frequency of the microbubble trapped inside the robot body cavity. (*A*) The experimental apparatus for exciting the microbubbles at different frequencies. (*i*) An array of microrobots with trapped microbubbles. (*ii*) The confocal image of the supporting polymeric shell. (*B*) The microstreaming pattern of the acoustically actuated microrobot at the resonance frequency of $f_{res} = 237$ kHz, while the swimmer's body is fixed and the orifice is parallel to the substrate (Movie S2). (*C*) The simulated acoustic pressure map at the resonance frequency, when the microrobot is immersed in a fluidic medium. (*D*) The average speeds of the 2-μm tracer particles at different frequencies, normalized by the piezoelectric sensor voltage. The averages are taken over 20 particles and the error bar represents the SD.

experimentally showed that, for spherical capsules containing a microbubble fixed on a pole, the streaming flow changes drastically as the pole height decreases from 30 μm to 10 μm, and recirculating streamlines appear around the capsule near the substrate. This complex microstreaming pattern close to the solid wall leads to complicated locomotion mechanisms. We observed that, immediately after sending acoustic waves, the free microrobots flip in such a way that the free oscillatory surface of the bubble at the orifice faces the substrate (Fig. 3*A* and Movie S4). We attribute this to the secondary Bjerknes force (34), meaning that the oscillating bubble attractively translates toward the rigid wall. Such translational force on the pulsating microbubble embedded in our microrobot is crucial as it produces a normal attractive force on the substrate (i.e., a compressive loading pressure to the surface), which keeps the robot on the surface while allowing the surface-slipping motion.

The microstreaming patterns around the microrobot create a net flux, allowing the slipping over the surface at very high speeds. We show that by using a small anisotropy in the structure of the microrobot the complex flow patterns can be controlled. Different from a previously reported mechanism (24), where active magnetic tilting of the microswimmers together with acoustic actuation are required for propulsion, the presence of the passive fin structure in our design enables unidirectional motion under pure acoustic actuation. We could observe the streaming jet by tracking a hinged microrobot immersed in a fluidic medium filled with 1-μm-diameter PS particles (Fig. 3*B* and Movie S5). It is worth noting that when the microrobot reorients its body under acoustic excitation and flips toward the substrate, the resulting streamlines in Fig. 3*B* are due to the combination of bubble oscillation and passive fin structure. However, the microstreaming pattern in Fig. 2*B* is mainly due to the bubble oscillation since the microrobots were fixed and their orifice faced in parallel to the substrate for resonance frequency characterization purposes.

The fin creates an anisotropy in the net streaming flow caused by the bubble oscillation, which is the fundamental mechanism for enabling the unidirectional propulsion in this work. A net unidirectional flux, essential for the control of swimming behavior,

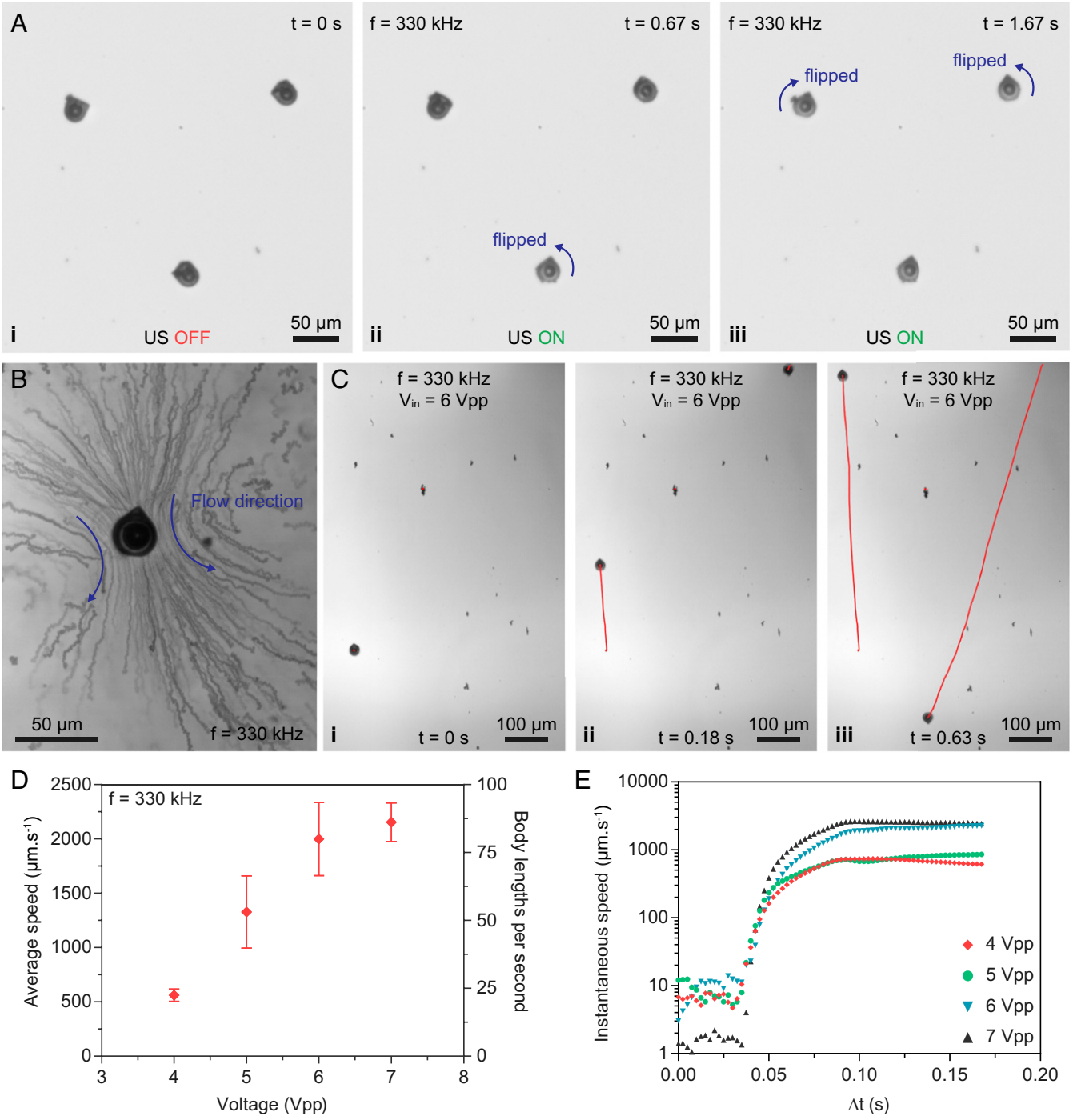

Fig. 3. Flipping and surface-slipping locomotion of the microrobots under acoustic actuation. (*A*) The released microrobot, actuated by the acoustic waves, flips in such a way that the oscillating free surface of the microbubble faces toward the solid substrate (Movie S3), where the driving voltage amplitude is 3.5 V_{pp}. (*i–iii*) Time-lapse images of three microrobots from starting position at t = 0 s to fully flipped orientation at t = 1.67 s. (*B*) The trajectory of 1-μm tracer particles following the jet streams around the microrobot after the flipping event; the blue arrows represent the streaming flow direction (Movie S5). (*C*) Two microrobots with different fin orientations slip forward (Movie S6). (*i–iii*) Time-lapse images of two oppositely moving microrobots from t = 0 s to t = 0.63 s. (*D*) The average speed of the robots under different acoustic voltage amplitudes, reaching up to 90 body lengths per second. Each data point represents the swimming speed analyzed from five microrobots. The error bar represents the SD. (*E*) The instantaneous speed associated with four different acoustic voltage levels (Movie S7). The rise time of the microrobots is around 0.05 s in order to reach their terminal speed.

allows the forward motion in the fin direction, as shown for two different microrobots in Fig. 3*C* and Movie S6. On the other hand, the fully symmetric design (Fig. 1*B*) behaves randomly as the translation and the self-rotation of the microrobot produces a trochoidal wavy motion (see the microrobot with the symmetric design in Movie S1), which is not desirable.

Next, in order to characterize the robot's swimming speed, we tracked the microrobots under ultrasound actuation with different driving voltage amplitudes. Fig. 3*D* presents the average speed of the surface-slipping microrobots for four different input voltages (Movie S7). A remarkable speed of around 2,300 μm/s, or equivalently 90 body lengths per second, was achieved at

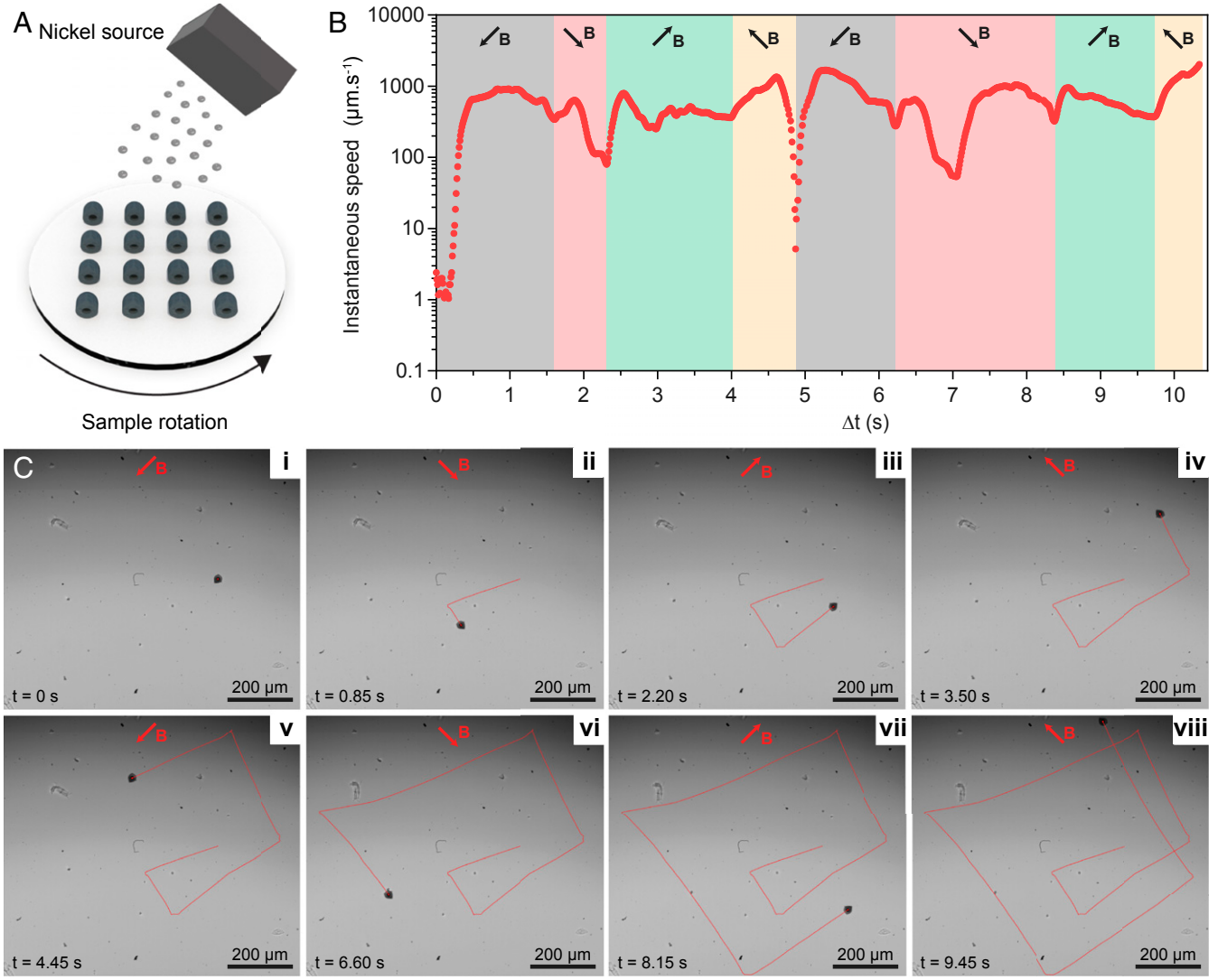

Fig. 4. Steering control of the microrobots under acoustic propulsion and magnetic field-based orientation control. (*A*) Sketch of the anisotropic magnetic nanofilm coating on the microrobots, where a 20-nm Ni nanofilm is directionally sputtered on the 3D-microprinted robots in the given specific orientation (i.e., the fin side is on the top). (*B*) The instantaneous speed of the magnetically steered microrobot under acoustic waves, plotted by the red dotted line, for eight turning events shown with time-lapse images in *C*, *i–viii*, where the red line indicates the trajectory of the microrobot (Movie S9). An in-plane magnetic field, with the direction indicated by B arrows, of 10-mT amplitude is applied to rotate the microrobots by 90°.

the low-Reynolds flow regime, thanks to the resonating microbubble engine. The Reynolds number $\mathrm{Re}=\rho VL/\mu$ for the swimming speed range of 1,000 to 2,300 μm/s is calculated to be between 0.03 and 0.07, where $\rho=1{,}005\ \mathrm{kg\cdot m^{-3}}$ and $\mu=8.90\times10^{-4}\mathrm{Pa\cdot s}$ are the density and the dynamic viscosity of the aqueous medium, respectively, and $L=30$ μm is the length scale of the microrobot. Although, the swimming occurs at low Reynolds number in the Stokes flow regime, the Reynolds number of the bubble motion (35) $\mathrm{Re_b}=\rho R_b^2\omega/\mu$ is around 190 for the bubble radius of $R_b=9$ μm and the excitation frequency of 330 kHz.

The high-speed swimming of the microrobot, at low Reynolds flow, arises from the nonlinear convection term in the Navier–Stokes equation, $\rho(u\cdot\nabla)u$, where ρ and u are the fluid density and flow speed, respectively. The nonlinear component indicates that the streaming flows around the microrobot are not necessarily symmetric, and thus the induced net momentum to the surr ounding flow causes the propulsion. By assuming swimming at low-Reynolds flow fields, we can estimate the propulsion force equal to the Stokes' drag as

$$F_p=F_D=6\pi\mu R_bV, \qquad [1]$$

where V is the terminal speed of the microrobot, and for $V\sim$ 1,000 to 2,300 μm/s the propulsion force F_p is in the range of ~0.2 to 0.6 nN. This is about two to three orders of magnitude higher than the thrust force of microorganisms such as algae (36) and bacteria (37) and is enough for the microrobot to move in vascular blood capillaries (38). Fig. 3*E* demonstrates the instantaneous speeds for four input voltage amplitudes. It is evident from the speed curves that their fast rise time allows the microrobots to reach the steady-state condition in less than 0.05 s. This fast acceleration adds extra controllability and sensitivity for navigating in confined 3D environments such as capillaries.

Notably, the acoustic radiation and streaming forces arising from the oscillating surface of the microbubble can attract

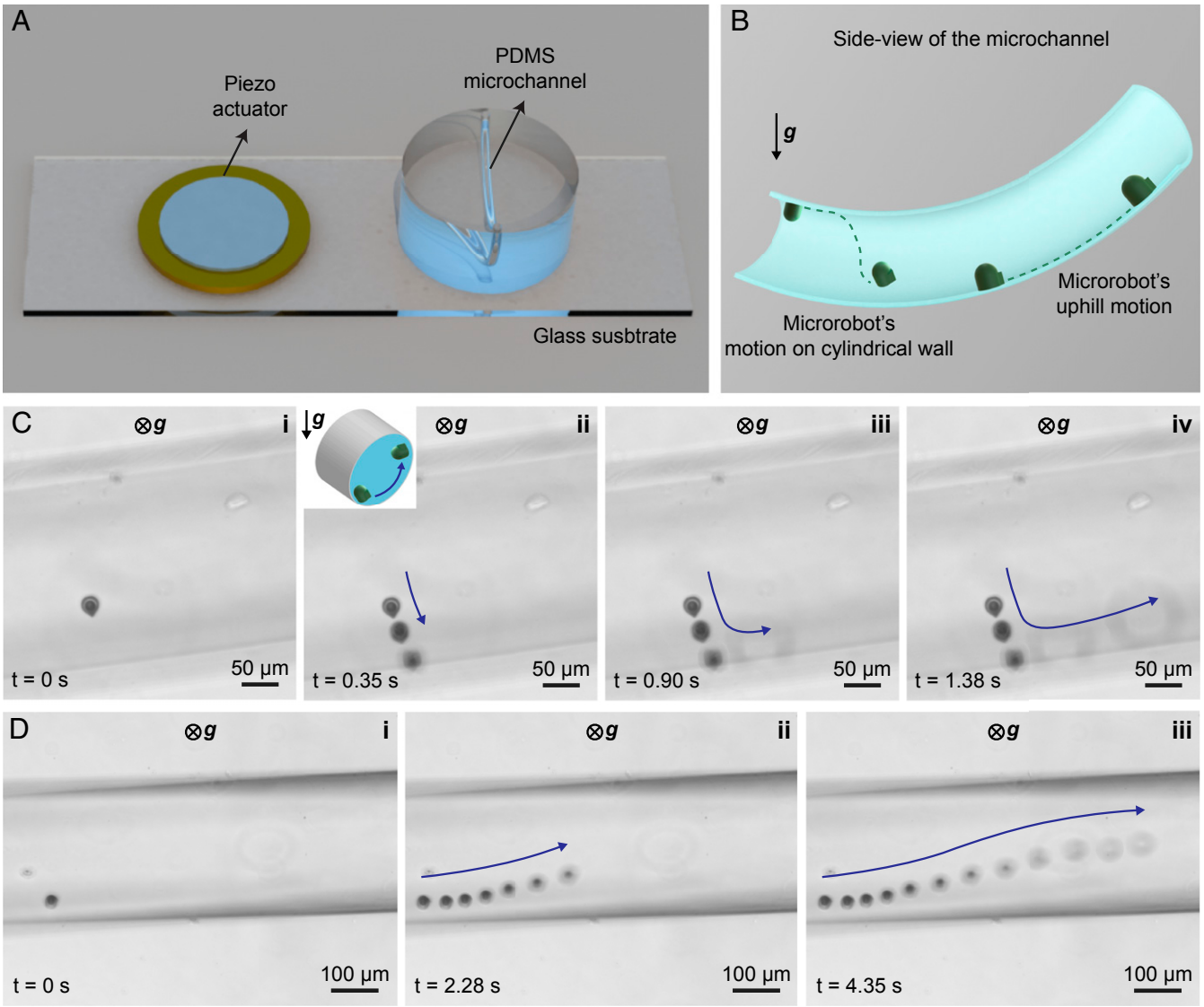

Fig. 5. Microrobot slipping on 3D curved surfaces. (*A*) Schematics of the experimental setup for actuation of the microrobots inside a circular channel of 300-μm diameter. (*B*) Sketch of the swimming behavior video snapshots on the curved walls. (*C*) The fin is oriented toward the cylindrical wall and, upon acoustic actuation, slips on the curved boundary and escapes the microscope focal plane. (*i–iv*) Time-lapse images of the surface-slipping motion of the microrobot, where the blue arrow indicates the locomotion direction. (*ii*, *Inset*) Schematics of the microrobot climbing the curved wall of circular cross-sectional channel. (*D*) The microrobot moves forward in length of the circular channel, under the applied ultrasound (Movie S10). (*i–iii*) Time-lapse images of the surface-slipping microrobot from the starting location at t = 0 s to t = 4.35 s, where the blue arrow indicates the motion direction. The symbols ↓*g* and ⊗*g* represent the downward and into-the-page gravity direction, respectively.

surrounding particles, depending on their volume and radius (39). Large particles with density higher than that of the medium are affected by the radiation force and become trapped to the resonating microbubble, whereas smaller particles tend to follow the acoustic vortex due to the streaming-induced drag force (40). Utilizing these phenomena, we demonstrated the trapping, transport, and release of 10-μm PS particles embedded in the fluid medium (*SI Appendix*, section S5 and Fig. S6 and Movie S8).

Magnetic Steering of the Acoustic Microrobots. The directional control of synthetic microrobots is important for their future medical applications such as targeted drug delivery. Therefore, to accomplish this steering control, we coated the microrobots with a 20-nm magnetic nickel (Ni) nanofilm by directional sputter coating, as shown schematically in Fig. 4*A*. The fin-up orientation of the microrobots after 3D printing allows an anisotropic magnetic coating, which facilitates the in-plane torque generation after the flipping (41). After the directional magnetic coating, we transferred the microrobots to a PDMS microchannel, which was placed under a custom-made coil setup, for combined actuation and control modalities using the acoustic and magnetic fields, respectively. Fig. 4*B* depicts the instantaneous speed of the acoustically actuated microrobot with magnetic steering under 10 s. There are eight sharp right-angle turning events, where we manually changed the magnetic **B** field (Fig. 4*C* and Movie S9). The average speed of the microrobot remains about 1 mm/s between the turning points. The deceleration and acceleration events due to change of the **B** field direction are marked in Fig. 4*B*. Again, the fast rise time allows the microrobot to move quickly in the desired direction. In addition, there are few slow-down motions between the turns, for instance at around 7 s, during which the adhesion to the substrate hinders the movement (Movie S9). Although the surface energy of

the glass substrate is not ideal, which is the case in real-life applications, the microrobot manages to escape the regions with high enough adhesion due to the surface-slipping mechanism and the large thrust force.

Locomotion on Curved 3D Surfaces. The majority of the work on the synthetic microrobots powered by magnetic and acoustic fields has focused on propulsion in 2D surfaces (2, 42). However, for the potential objective of cargo and drug delivery inside confined spaces of the human body, the microrobots should be able to propel on 3D tissue surfaces. Swimming near the vessel walls is an efficient type of propulsion that many biological microorganisms, such as neutrophils, macrophages, and white blood cells, use to avoid the high-speed blood flow (43). Most recently, Ahmed et al. (44) proposed a neutrophil-inspired propulsion mechanism based on combined acoustic and magnetic actuations. They showed that using an acoustic radiation force the superparamagnetic nanoparticles, which form aggregates under the rotational magnetic field, migrate to the boundaries of the channel, and thus use rolling on the wall to propel.

Unlike the previously reported work (44) where a global acoustic pressure gradient is required to push the lump magnetic particles to the wall, our microrobot can locally be attracted to the boundaries only because of the oscillatory layer of the confined microbubble. Here, we demonstrated the surface slipping of the microbubble-based microrobot on curved boundaries inside circular channels (Movie S10). Under ultrasound actuation (with the experimental setup shown in Fig. 5*A*), the microrobot was slipping over the curved surface as shown in Fig. 5 *B–D*. Depending on the orientation of the fin, which can be controlled with the magnetic field, the microrobot could slide very close to the wall and move forward even against gravity.

Discussion

Untethered synthetic microrobots have raised significant interest in biomedical and laboratory-on-a-chip applications due to their wireless actuation and precise control capabilities. Most of the artificial microrobots typically follow the "scallop theorem" and employ low-Reynolds flow design guidelines to create the nonreciprocal motion of the moving part (45). Such examples are the microscale sperm-inspired undulating flagella (46) and bacterial flagella-inspired corkscrew motion (47). In this study, we demonstrate a different propulsion strategy at low-Reynolds flow regime that allows fast and directional surface-slipping motion. The periodic oscillation of the trapped microbubble inside the polymeric shell, with an anisotropic geometry, allows two main functions: 1) attraction toward the solid boundaries (flat or curved surfaces) and 2) generation of axisymmetric microstreaming flow, which enables a unidirectional slipping motion at high speed. These capacities would allow the microrobot to potentially move within capillaries, where the flow is laminar and has average speed on the order of 1 mm/s (38). Moreover, the flow speed close to the vessel walls decreases drastically in the case of laminar flow, and thus slipping motion of the proposed microrobots close to the surface would be beneficial. The surface of the microrobots can be functionalized using receptors to target specific cells in the biological environments (48). Further, the body of microrobots can be modified with different materials, such as gelatin and fibronectin, to encapsulate cargo (e.g., drugs) to deliver it in target locations precisely (18, 49).

On the other hand, the assembly and disassembly of the acoustic microrobots would be possible, due to the mutual multibubble interactions resulting from the secondary order Bjerknes force (34, 50). In addition to the actuation and control strategies, the real-time imaging of the microscopic swimmers presents a grand challenge in the microrobotics field. However, the presence of the microbubbles inside the microrobots would allow their detection under well-established ultrasound imaging techniques, similar to the application of contrast agents (51). Furthermore, the acoustic microrobots can be recruited for microbubble-mediated blood–brain barrier treatments (52), where the trapped microbubbles can be oscillated by focused ultrasound waves after reaching the target location. Future work will explore the stability of microbubbles in biological fluids and the collective motion of the microrobots for complicated medical tasks under the application of acoustic and magnetic fields.

Materials and Methods

Fabrication of the Microrobots. Microrobots were 3D-microprinted using a commercially available two-photon polymerization system (Photonic Professional GT, Nanoscribe GmbHany) with a 63× oil-immersion objective (numerical aperture = 1.4). The optimum microrobot fabrication with proper spherical cavity was realized using 15° hatching angle offset with 23 mW laser power and 5.0×10^5 μm galvanometric mirror *x*- and *y*- scanning speeds. Following fabrication, the microrobots were developed with propylene glycol methyl ether acetate solution for 30 min to fully remove the remaining resin inside the spherical cavity and then stored in isopropanol. The microrobots were detached from the substrate prior to each experiment using a tweezer and transferred into the channels using 3% (wt/vol) Pluronic in double-distilled H_2O-coated micropipette tips.

Imaging of the Acoustic Microrobots. The microrobots were initially characterized with an inverted optical microscope (Nikon Instruments) to investigate the proper formation of the cavities and to examine the entrapment of the air bubble into these cavities. The microrobot images under Nikon microscope were captured by Hamamatsu Orca Flash4 camera (Hamamatsu Photonics). For bubble resonance characterizations, the images were taken using a high-speed camera (M310; Phantom, Inc.) with 1,000 frames per second, and for the swimming speed, 100 to 400 frames per second were used. The images were then analyzed using a custom-made Python code.

Finite Element Simulations. The finite element simulations were carried out using the acoustics–solid interaction module of Comsol Multiphysics 5.4 (COMSOL, Inc.). A 2D axisymmetric geometric model of the acoustic microrobot was developed. The spherical air bubble was introduced inside the polymeric shell body, and the whole structure was immersed in a fluidic media. A plane wave radiation boundary condition was set to the outer boundaries and an incident acoustic pressure wave of 1 kPa was defined at one edge of the medium. Then, the eigenfrequency analysis was conducted to obtain the resonance frequency of the spherical bubble.

The Acoustic Setup for Characterization and Actuation of the Microrobots. For characterizing the resonant frequency of the trapped microbubbles, a PDMS microchannel was fabricated using a standard soft lithography procedure and bonded on the glass slide after oxygen plasma treatment. A piezoelectric disk transducer was then bonded adjacent to the PDMS microchannel and connected to a function generator (AFG3102C; Tektronix, Inc.) for sinusoidal actuation purposes. For swimming tests, a similar setup was used but with a PDMS cell to transfer the microrobots and a PDMS cap to close the chamber. The use of acoustically transparent material for the test chamber helps to avoid the generation of standing wave.

Data Availability. The custom-made Python codes and other data that support the findings of this study are available from the corresponding author upon request.

ACKNOWLEDGMENTS. This work is funded by the Max Planck Society.

1. K. E. Peyer, S. Tottori, F. Qiu, L. Zhang, B. J. Nelson, Magnetic helical micromachines. *Chemistry* **19**, 28–38 (2013).
2. M. Sitti *et al.*, Biomedical applications of untethered mobile milli/microrobots. *Proc IEEE Inst. Electr. Electron. Eng.* **103**, 205–224 (2015).
3. J. Li, B. Esteban-Fernández de Ávila, W. Gao, L. Zhang, J. Wang, Micro/nanorobots for biomedicine: Delivery, surgery, sensing, and detoxification. *Sci. Robot.* **2**, 1–9 (2017).
4. P. Erkoc *et al.*, Mobile microrobots for active therapeutic delivery. *Adv. Ther.* **2**, 1800064 (2019).
5. B. Dai *et al.*, Programmable artificial phototactic microswimmer. *Nat. Nanotechnol.* **11**, 1087–1092 (2016).
6. V. Sridhar, B. W. Park, M. Sitti, Light-driven Janus hollow mesoporous TiO2–Au microswimmers. *Adv. Funct. Mater.* **28**, 1704902 (2018).

7. A. Aubret, M. Youssef, S. Sacanna, J. Palacci, Targeted assembly and synchronization of self-spinning microgears. *Nat. Phys.* **14**, 1114–1118 (2018).
8. Y. Klapper, N. Sinha, T. W. S. Ng, D. Lubrich, A rotational DNA nanomotor driven by an externally controlled electric field. *Small* **6**, 44–47 (2010).
9. Y. Alapan, B. Yigit, O. Beker, A. F. Demirörs, M. Sitti, Shape-encoded dynamic assembly of mobile micromachines. *Nat. Mater.* **18**, 1244–1251 (2019).
10. U. Bozuyuk *et al*., Light-triggered drug release from 3D-printed magnetic chitosan microswimmers. *ACS Nano* **12**, 9617–9625 (2018).
11. H. Ceylan *et al*., 3D-printed biodegradable microswimmer for theranostic cargo delivery and release. *ACS Nano* **13**, 3353–3362 (2019).
12. D. Ahmed *et al*., Selectively manipulable acoustic-powered microswimmers. *Sci. Rep.* **5**, 9744 (2015).
13. J. F. Louf, N. Bertin, B. Dollet, O. Stephan, P. Marmottant, Hovering microswimmers exhibit ultrafast motion to navigate under acoustic forces. *Adv. Mater. Interfaces* **5**, 1800425 (2018).
14. J. R. Howse *et al*., Self-motile colloidal particles: From directed propulsion to random walk. *Phys. Rev. Lett.* **99**, 048102 (2007).
15. B. E.-F. de Ávila *et al*., Micromotor-enabled active drug delivery for in vivo treatment of stomach infection. *Nat. Commun.* **8**, 272 (2017).
16. N. Riley, Steady streaming. *Annu. Rev. Fluid Mech.* **33**, 43–65 (2001).
17. S. Tottori *et al*., Magnetic helical micromachines: Fabrication, controlled swimming, and cargo transport. *Adv. Mater.* **24**, 811–816 (2012).
18. I. C. Yasa, A. F. Tabak, O. Yasa, H. Ceylan, M. Sitti, 3D-Printed microrobotic transporters with recapitulated stem cell niche for programmable and active cell delivery. *Adv. Funct. Mater.* **29**, 1808992 (2019).
19. T. Leighton, *The Acoustic Bubble* (Academic Press, 2012).
20. J. Feng, J. Yuan, S. K. Cho, 2-D steering and propelling of acoustic bubble-powered microswimmers. *Lab Chip* **16**, 2317–2325 (2016).
21. J. Feng, J. Yuan, S. K. Cho, Micropropulsion by an acoustic bubble for navigating microfluidic spaces. *Lab Chip* **15**, 1554–1562 (2015).
22. D. Ahmed, C. Dillinger, A. Hong, B. J. Nelson, Artificial acousto-magnetic soft microswimmers. *Adv. Mater. Technol.* **2**, 1700050 (2017).
23. N. Bertin *et al*., Propulsion of bubble-based acoustic microswimmers. *Phys. Rev. Appl.* **4**, 064012 (2015).
24. L. Ren *et al*., 3D steerable, acoustically powered microswimmers for single-particle manipulation. *Sci. Adv.* **5**, eaax3084 (2019).
25. C. Eckart, Vortices and streams caused by sound waves. *Phys. Rev.* **73**, 68–76 (1948).
26. W. L. Nyborg, Acoustic streaming near a boundary. *J. Acoust. Soc. Am.* **30**, 329–339 (1958).
27. S. A. Elder, Cavitation microstreaming. *J. Acoust. Soc. Am.* **31**, 54–64 (1959).
28. T. M. Squires, S. R. Quake, Microfluidics: Fluid physics at the nanoliter scale. *Rev. Mod. Phys.* **77**, 977–1026 (2005).
29. J. C. Rife *et al*., Miniature valveless ultrasonic pumps and mixers. *Sens. Actuators A Phys.* **86**, 135–140 (2000).
30. T. Qiu *et al*., Wireless acoustic-surface actuators for miniaturized endoscopes. *ACS Appl. Mater. Interfaces* **9**, 42536–42543 (2017).
31. H. Bruus, Acoustofluidics 7: The acoustic radiation force on small particles. *Lab Chip* **12**, 1014–1021 (2012).
32. S. Ozeri, D. Shmilovitz, Ultrasonic transcutaneous energy transfer for powering implanted devices. *Ultrasonics* **50**, 556–566 (2010).
33. A. A. Doinikov, A. Bouakaz, Effect of a distant rigid wall on microstreaming generated by an acoustically driven gas bubble. *J. Fluid Mech.* **742**, 425–445 (2014).
34. L. A. Crum, Bjerknes forces on bubbles in a stationary sound field. *J. Acoust. Soc. Am.* **57**, 1363–1370 (1975).
35. N. Mobadersany, K. Sarkar, Acoustic microstreaming near a plane wall due to a pulsating free or coated bubble: Velocity, vorticity and closed streamlines. *J. Fluid Mech.* **875**, 781–806 (2019).
36. O. Yasa, P. Erkoc, Y. Alapan, M. Sitti, Microalga-powered microswimmers toward active cargo delivery. *Adv. Mater.* **30**, e1804130 (2018).
37. M. R. Edwards, R. Wright Carlsen, M. Sitti, Near and far-wall effects on the three-dimensional motion of bacteria-driven microbeads. *Appl. Phys. Lett.* **102**, 143701 (2013).
38. B. J. Nelson, I. K. Kaliakatsos, J. J. Abbott, Microrobots for minimally invasive medicine. *Annu. Rev. Biomed. Eng.* **12**, 55–85 (2010).
39. D. Ahmed *et al*., Rotational manipulation of single cells and organisms using acoustic waves. *Nat. Commun.* **7**, 11085 (2016).
40. D. L. Miller, Particle gathering and microstreaming near ultrasonically activated gas-filled micropores. *J. Acoust. Soc. Am.* **84**, 1378–1387 (1988).
41. P. Tierno, Recent advances in anisotropic magnetic colloids: Realization, assembly and applications. *Phys. Chem. Chem. Phys.* **16**, 23515–23528 (2014).
42. X. Z. Chen *et al*., Small-scale machines driven by external power sources. *Adv. Mater.* **30**, e1705061 (2018).
43. P. Friedl, B. Weigelin, Interstitial leukocyte migration and immune function. *Nat. Immunol.* **9**, 960–969 (2008).
44. D. Ahmed *et al*., Neutrophil-inspired propulsion in a combined acoustic and magnetic field. *Nat. Commun.* **8**, 770 (2017).
45. H.-W. Huang, M. S. Sakar, A. J. Petruska, S. Pané, B. J. Nelson, Soft micromachines with programmable motility and morphology. *Nat. Commun.* **7**, 12263 (2016).
46. B. J. Williams, S. V. Anand, J. Rajagopalan, M. T. A. Saif, A self-propelled biohybrid swimmer at low Reynolds number. *Nat. Commun.* **5**, 3081 (2014).
47. L. Zhang *et al*., Characterizing the swimming properties of artificial bacterial flagella. *Nano Lett.* **9**, 3663–3667 (2009).
48. V. Garcia-Gradilla *et al*., Functionalized ultrasound-propelled magnetically guided nanomotors: Toward practical biomedical applications. *ACS Nano* **7**, 9232–9240 (2013).
49. H. Ceylan, I. C. Yasa, M. Sitti, 3D chemical patterning of micromaterials for encoded functionality. *Adv. Mater.* **29**, 1605072 (2017).
50. J. G. S. Moo *et al*., Bjerknes forces in motion: Long-range translational motion and chiral directionality switching in bubble-propelled micromotors via an ultrasonic pathway. *Adv. Funct. Mater.* **28**, 1702618 (2018).
51. K. Ferrara, R. Pollard, M. Borden, Ultrasound microbubble contrast agents: Fundamentals and application to gene and drug delivery. *Annu. Rev. Biomed. Eng.* **9**, 415–447 (2007).
52. R. M. Jones *et al*., Three-dimensional transcranial microbubble imaging for guiding volumetric ultrasound-mediated blood-brain barrier opening. *Theranostics* **8**, 2909–2926 (2018).